Journal of Materials Chemistry A

ROYAL SOCIETY OF CHEMISTRY

PAPER

View Article Online
View Journal | View Issue

Cite this: J. Mater. Chem. A, 2024, 12, 6983

Sulfur-doped cobalt molybdenum oxide with a hydrangea-like structure for bi-functionally efficient overall water splitting†

Jie Dong, [a] Saiyi Chen,[a] Cuncai Lv, [b] Mark G. Humphrey, [c] Chi Zhang *[a] and Zhipeng Huang *[a]

Developing an efficient bi-functional water-splitting catalyst is crucial for advancing sustainable hydrogen energy applications. A novel sulfur-doped cobalt molybdenum oxide (CoMoO) catalyst with a hydrangea-like structure was synthesized *in situ* on a carbon fiber paper substrate using a simple one-step hydrothermal process. The optimized sample exhibits excellent hydrogen evolution reaction (HER) and oxygen evolution reaction (OER) catalytic activity with an overpotential of 105 and 205 mV at a current density of 10 mA cm^{-2} under alkaline conditions, respectively. Experimental characterization shows that the introduction of sulfur efficiently modifies the composition and morphology of the CoMoO electrocatalyst, which increases the electrochemically active surface area and improves the electrocatalytic kinetics. The improved electrocatalytic performance can be attributed to the synergistic effects of the various metal ion constituents. Mo^{4+} enhances water adsorption and accelerates the reaction kinetics of H_2 generation from Co^{2+} or S_n^{2-}. Meanwhile, S_n^{2-} can accelerate the charge transfer, facilitating the OER process. Additionally, the presence of Mo^{4+} contributes to the stabilization of OER intermediates, thereby enhancing the efficiency of the OER process on CoOOH active sites. The hydrangea-like structure also offers plentiful active sites and efficient mass transfer. Besides, this electrolyzer obtains a current density of 10 mA cm^{-2} at a cell voltage of 1.61 V.

Received 29th November 2023
Accepted 8th January 2024

DOI: 10.1039/d3ta07380g

rsc.li/materials-a

1. Introduction

The global shift from fossil fuels to renewable energy sources is imperative for meeting energy demands and ensuring sustainable living conditions.[1–3] In this context, the hydrogen evolution reaction (HER) and oxygen evolution reaction (OER) have emerged as pivotal processes for producing green hydrogen from renewable sources through water electrolysis.[4–9] Developing bi-functional electrocatalysts capable of enhancing the slow kinetics of both the HER and the OER is essential for efficient overall water splitting.[10,11] Despite significant efforts to develop effective electrocatalysts, most reported catalysts specialize in the OER or HER.[10] This is mainly due to the enormous challenge of producing dual functionality within a single catalyst and the severe activity decay that limits application at scale.[11,12] The specific reasons may be as follows: the distinct mechanisms and activity requirements of the HER and OER present hurdles in designing a catalyst promoting both processes.[13] Second, multistep reactions involving complex electron and proton transfers often limit reaction rates, emphasizing the need to consider kinetic limitations when designing bi-functional catalysts.[14] Additionally, modulating the active sites on the catalyst surface to meet the requirements of both the HER and the OER is critical.[14] Moreover, achieving durability and stability in a bi-functional catalyst poses a significant challenge. In addition, the cost, scarcity, and durability issues of precious metal catalysts (Pt and IrO_2/RuO_2) restrict their widespread practical application.[15–17] Therefore, finding a low-cost yet efficient non-precious metal bi-functional electrocatalyst is of great importance for developing the hydrogen economy.

Transition metal-based catalysts have been extensively studied for efficient electrolysis technology due to their low cost, abundance, low toxicity, and high activity.[18–22] In particular, bimetallic oxide catalysts have shown promise due to their multiple oxidation states, structural stability, unique electronic structures, and abundant defects, making them highly suitable for bi-functional HER and OER electrocatalysis.[23–25] Among them, the bimetallic oxide $CoMoO_4$ is a promising material with

[a]China-Australia Joint Research Center for Functional Molecular Materials, School of Chemical Science and Engineering, Tongji University, Shanghai, 200092, China. E-mail: chizhang@tongji.edu.cn; zphuang@tongji.edu.cn

[b]Key Laboratory of High-precision Computation and Application of Quantum Field Theory of Hebei Province, Hebei Key Lab of Optic-electronic Information and Materials, The College of Physics Science and Technology, Hebei University, Baoding 071002, China

[c]Research School of Chemistry, Australian National University, Canberra, ACT, 2601, Australia

† Electronic supplementary information (ESI) available. See DOI: https://doi.org/10.1039/d3ta07380g

good intrinsic activity. Introducing the high-valent metal Mo into $CoMoO_4$ can modulate the electronic structure of Co, improve electrical conductivity, and optimize water-splitting intermediate's adsorption energy, thereby enhancing catalytic performance.[26–28] Therefore, developing bimetallic oxides with multifunctional catalytic properties is currently a hot topic in energy-related fields.

Non-metallic element doping effectively optimizes catalytic performance by modulating the electronic structure, enhancing wettability, lowering the kinetic energy barrier, and introducing additional active sites.[29–32] Pang's work involved the introduction of nitrogen doping to enhance the electronic conductivity and OH adsorption strength of Co_3O_4, resulting in accelerated reaction kinetics and improved catalytic activity for the OER.[33] Liu's research group has shown that phosphorus doping optimizes the electronic configuration and enhances the valence state of iron ions.[34] This results in a nearly twofold increase in the mass and specific activity of $LaFeO_{3-\delta}$.[34] Similar to doping with P or N, sulfur doping can also improve the electrochemical performance of metal oxides.[32] Sulfur doping can replace oxygen atoms to improve intrinsic conductivity and introduce abundant oxygen vacancies to provide enough catalytically active sites.[32] Inspired by these findings, we aim to explore the potential of introducing S into cobalt molybdate to enhance the performance of the HER and OER further. However, the direct synthesis of metal oxides doped with non-metallic elements through these strategies still poses challenges due to the requirement of additional reactions with compounds containing heteroatoms. The synthesis of heteroatoms also suffers from drawbacks such as using toxic precursors, complex processes, and releasing toxic gases (H_2S, PH_3, *etc.*). While extensive studies have shown the benefits of doping non-metallic elements in metal oxides to improve electrochemical and electrocatalytic properties, there is limited literature regarding sulfur doping.

Based on the above discussion, we synthesised a bifunctional S-doped cobalt molybdate (S-CoMoO-12.4) electrocatalyst on carbon fiber paper (CFP) by a simple one-step hydrothermal method. Such a catalyst possesses a hydrangea-like structure with a large specific surface area and rapid mass transfer capabilities. As expected, S-CoMoO-12.4 demonstrates ultralow overpotentials of 105 and 205 mV at a current density of 10 mA cm^{-2} in alkaline HER and OER processes, respectively. The experimental results show that introducing sulfur could effectively tune the electrocatalyst composition and morphology, increase the electrochemically active surface area and improve the electrocatalytic kinetics. The improved electrocatalytic performance can be attributed to the synergistic effects of the various ion constituents. Mo^{4+} as a reactant adsorption site enhances the adsorption of H_2O molecules, thereby promoting the occurrence of the HER in the Co^{2+} or S_n^{2-} site. Moreover, Mo^{4+} facilitates the attraction of electrons from the OER intermediate, stabilizing the intermediate and enhancing OER activity. S_n^{2-} species also promote the OER processes, attributed to their ability to accelerate charge transfer. A two-electrode electrolyzer achieves 10 mA cm^{-2} with a cell voltage of 1.61 V for overall water splitting in 1.0 M KOH. This work presents a promising strategy for rationalizing and synthesizing efficient bimetallic electrocatalysts.

2. Experimental section

2.1 Synthesis of S-CoMoO and CoMoO

The CFP undergoes a pretreatment process involving hydrochloric and nitric acid (the volume ratio is 1 : 1) to enhance its hydrophilicity and eliminate impurities. Subsequently, the paper is subjected to sequential ultrasonic cleaning with acetone, C_2H_5OH, and deionized H_2O for 15 minutes each to eliminate greasy dirt from its surface. Following this, the CFP is dried in a drying oven.

The synthesis of S-CoMoO-12.4 was carried out using a one-step hydrothermal method. In a beaker, 3.0 mmol of $Co(NO_3)_2 \cdot 6H_2O$, 15.0 mmol of urea, 3.6 mmol of $(NH_4)_6Mo_7O_{24} \cdot 4H_2O$, and 37.3 mmol of thiourea are initially dissolved in 80 mL of deionized water, along with 6.0 mmol of NH_4F. Magnetic stirring is applied to the mixture for 30 minutes before transferring it to a 150 mL Teflon-lined autoclave containing a CFP (3 cm × 6 cm). The autoclave is sealed, and the temperature is gradually raised at a rate of 1.5 °C min^{-1} to reach 120 °C, which is maintained for 7 h. Subsequently, the temperature is presented at a rate of 1.3 °C min^{-1} to 200 °C and held there for 8 h. Finally, the autoclave is allowed to cool to room temperature, and the synthesized S-CoMoO is washed with deionized H_2O and C_2H_5OH. S-CoMoO-*R* (R = 3.1, 6.2, 9.3, 15.5, 18.6, representing the feeding atomic ratio of S/Co) is utilized as a control sample. The synthesis of CoMoO follows a similar procedure to that of S-CoMoO, except that thiourea is not included in the initial feedstock.

2.2 Characterization

X-ray diffraction (XRD) analysis was conducted using a D8 Advance diffractometer (Bruker, Germany), and scanning electron microscopy (SEM) observations were performed with a JSM-7900F device (JEOL, Japan). Transmission electron microscopy (TEM) images were obtained using a Talos F200S G2 (Thermo Fisher, USA). X-ray photoelectron spectroscopy (XPS) data were collected using an ESCALAB Xi+ photoelectron spectrometer (Thermo Fisher, USA). The N_2 adsorption–desorption isotherms were recorded using a BSD-PM specific surface and microporous analyzer (Beishide Instrument, China).

2.3 Electrochemical measurements

The electrochemical measurements were performed on a CHI 760E electrochemical workstation with a standard three-electrode system. S-CoMoO-*R* is the working electrode, a carbon rod is the counter electrode, and a $Hg/HgO/OH^-$ electrode is the reference electrode. All measured potentials were calibrated to a reversible hydrogen electrode (RHE). Polarization curves were obtained using linear scanning voltammetry (LSV) for the OER in a 1.0 M KOH solution, with a scan rate of 5 mV s^{-1} and 80% of the *iR* drop compensated for the OER and HER measurements. Electrochemical impedance spectroscopy (EIS) measurements were carried out at voltages of

−0.21 and 1.53 V *vs.* RHE with a bias of 5 mV and a frequency range of 100 kHz to 0.01 Hz. Long-term durability tests were performed using chronopotentiometry measurements without compensation for the *iR* drop. Tafel plots were generated by plotting the overpotential as a function of current density in logarithmic terms. The Tafel slope, calculated using the equation $\eta = a + b\log|j|$, where η is the overpotential, a is the Tafel constant, b is the Tafel slope, and j is the current density, was used to assess the kinetics of the HER. The turnover frequency (TOF) was calculated using the equation $\mathrm{TOF} = (j \times A)/(z \times F \times n)$, where j represents the current density at a given overpotential (*e.g.*, $\eta = 300$ mV), A is the surface area of the working electrode, z represents the number of electrons transferred to produce one molecule of the target product (with a value of 2 for the HER and 4 for the OER), F is the Faraday constant, and n is the amount of substance of active material (moles). Assuming Co sites are more active than Mo sites, a conservative estimate of n is the total number of moles of all Co atoms in S-CoMoO-12.4. CoMoO, S-CoMoO-12.4, Pt/C and RuO_2 loading in the electrochemical measurement was 1.50, 1.46, 1.50 and 1.50 mg cm^{-2}.

3. Results and discussion

3.1 Compositions and structures

As illustrated in Fig. 1, the synthesis of S-CoMoO-12.4 involves a one-step hydrothermal reaction using cobalt nitrate, thiourea, and ammonium molybdate as the sources of cobalt, sulfur, and molybdenum, respectively. The reaction takes place in an aqueous solution containing urea and ammonium fluoride. Fig. 2a shows the XRD patterns of the prepared S-CoMoO-12.4 with characteristic diffraction peaks at 9.6°, 12.0°, 17.1°, 23.4°, 29.2°, 46.8° and 54.5° belonging to $Co_{1.2}MoO_{4.2}\cdot 1.3H_2O$ (PDF#14-0087), indicating that the S-doping retains the crystal structure of $Co_{1.2}MoO_{4.2}$. In addition, un-doped CoMoO is synthesised using a similar method and its XRD pattern is consistent with PDF#14-0087 (Fig. 2a). Notably, the intensity of the CoMoO diffraction peaks decreases with an increase in the feeding atomic ratio of S/Co, suggesting that S doping of CoMoO leads to reduced crystallinity. The XRD pattern also includes a diffraction peak of spades (Fig. 2a) at 26.5° attributed to the CFP substrate. In addition, the dominance of the CFP substrate peaks in the XRD pattern also indicates the low crystallinity of the samples grown on CFP through hydrothermal synthesis.

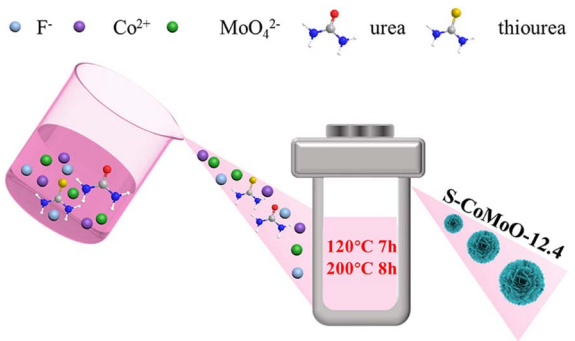

Fig. 1 Schematic diagram of the synthesis process of S-CoMoO-12.4.

The typical morphology of S-CoMoO samples is shown in Fig. S1.† At low R, the nanosheets (thickness approximately 37 nm) were randomly arranged on the CFP surface (Fig. S1a†). As the R increases, the nanosheet thickness in S-CoMoO-6.2 (Fig. S1b†) becomes nearly twice that in S-CoMoO-3.1. In addition, these nanosheets self-assemble into microspheres with an average diameter of about 2.4 μm. However, as the R increases, the nanosheets transition from self-assembled microspheres to varying-sized cubes, as observed in Fig. S1c.† As R continues to grow, the S-CoMoO-12.4 catalyst exhibited a morphology resembling hydrangea-like microspheres with an average diameter of approximately 1.9 μm (Fig. 2b and c). Nevertheless, a high R leads to a blocky cobalt molybdate morphology (Fig. S1e and f†), significantly reducing the surface area. Also, the Brunauer–Emmett–Teller (BET) surface area (Fig. S2†) of CoMoO-15.5 (12.5 m^2 g^{-1}) and CoMoO-18.6 (6.7 m^2 g^{-1}) is smaller than that of CoMoO-12.4 (38.5 m^2 g^{-1}) (Fig. S3a†). The SEM images demonstrate the significant influence of R on the morphology of cobalt molybdate. Varied S/Co feeding atomic ratios can influence the growth and self-assembly of CoMoO nanosheets, thereby offering a means to adjust the structure and morphology of CoMoO and enhance its catalytic performance. To better understand how the actual sulfur levels affect their morphology, we used energy dispersive X-ray (EDX) spectroscopy to determine their elemental contents (Fig. S3b, S4 and Table S1†), the results of which are shown in Fig. S3b, S4 and Table S1.† The TEM image (Fig. 2d) of S-CoMoO-12.4 shows the structure to be an embroidered spherical structure with an average diameter of 2.0 μm, consistent with the SEM results. In addition, the high-resolution TEM (HRTEM) images (Fig. 2e–i) of S-CoMoO-12.4 reveal two distinct lattice stripes with lattice spacings of 0.32 and 0.20 nm, corresponding to the XRD results at 29.2° and 46.8° of S-CoMoO-12.4. The high-angle annular dark field scanning transmission electron microscopy (HAADF-STEM) images and synchronous EDX mapping (Fig. 2j) show that Co, S, Mo, and O elements are uniformly distributed throughout the entire sample, further confirming successful sulfur doping.

XPS was employed to reveal further the effect of S doping on the sample's electronic structure. The XPS analysis investigated the chemical composition and element states in Fig. 3 and S5.† The survey spectrum (Fig. S5†) indicates the presence of Co, S, Mo, and O elements in the S-CoMoO-12.4 sample. The C 1s peak at 284.8 eV was used as the XPS correction peak. The Co 2p XPS spectrum of S-CoMoO-12.4 (Fig. 3a) exhibited peaks at binding energies near 781.8 and 797.6 eV, corresponding to the Co $2p_{3/2}$ and Co $2p_{1/2}$ energy levels. In addition, the binding energy difference between Co $2p_{3/2}$ and Co $2p_{1/2}$ is 15.8 eV, a sign of the Co^{2+} oxidation state.[35,36] Satellite peaks were observed at 786.4 and 802.8 eV. With the incorporation of S, a group of new peaks at 779.5 (Co $2p_{3/2}$) and 794.3 eV (Co $2p_{1/2}$) appeared, indicating the presence of trivalent cobalt in S-CoMoO-12.4.[37,38] This observation indicates that the highly electronegative O atom is partly substituted by the less electronegative S atom, leading to

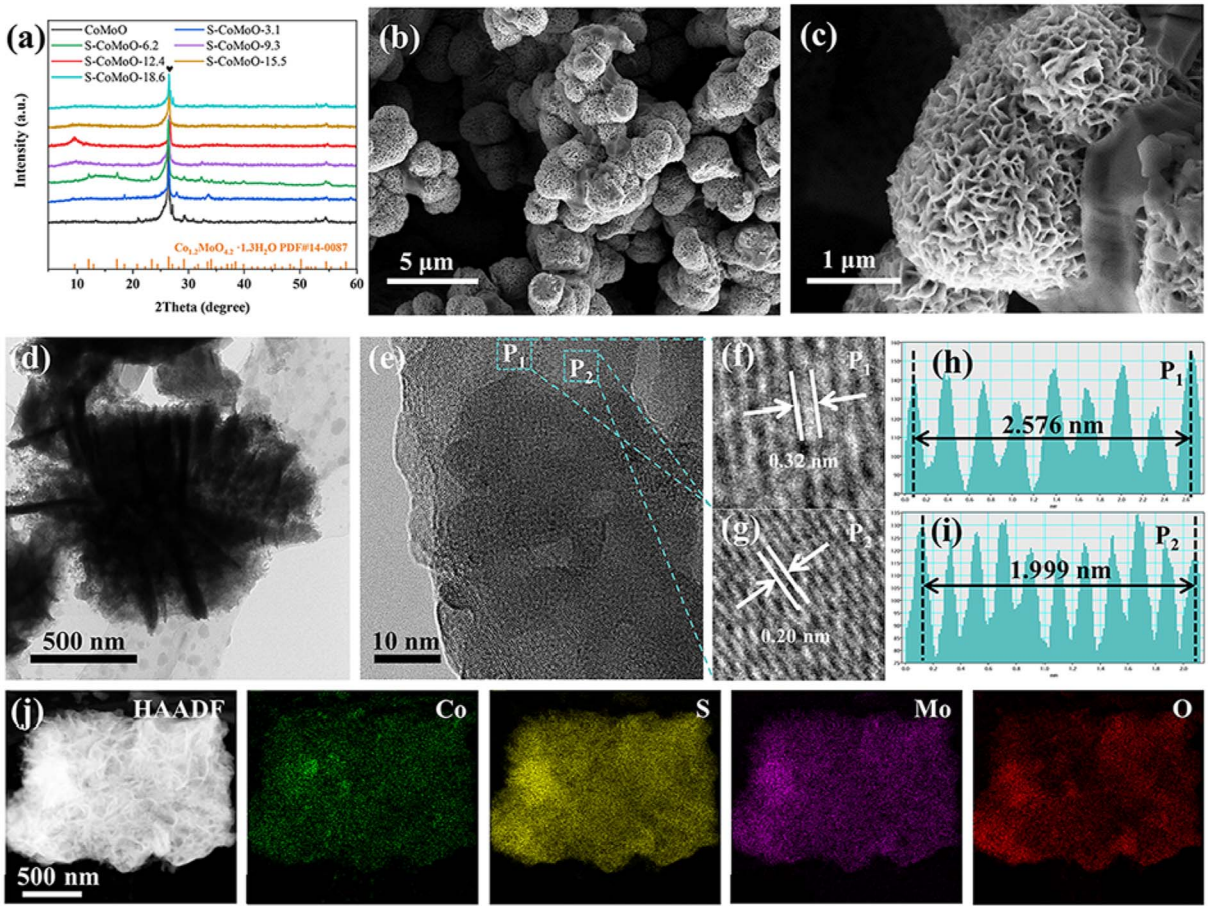

Fig. 2 (a) XRD patterns of CoMoO and S-CoMoO-*R* (*R* = 3.1, 6.2, 9.3, 12.4, 15.5 and 18.6) samples; (b and c) SEM images; (d) TEM images; (e–g) HRTEM images; (h and i) line contour maps corresponding to (f) and (g); (j) HAADF-STEM maps and corresponding EDX elemental mappings for S-CoMoO-12.4.

the non-metallic atom being less attractive to the electrons of the metal Co atom, causing the Co atom to be more prone to losing electrons and thus increasing its oxidation state.[39] In the Mo 3d spectrum of S-CoMoO-12.4 (Fig. 3b), two peaks at 233.0 and 236.1 eV can be deconvoluted, attributed to Mo $3d_{5/2}$ and Mo $3d_{3/2}$, respectively. The width between these spin–orbit split peaks is 3.1 eV, suggesting that Mo 3d is the same as Mo^{6+}.[40,41] Additionally, the appearance of two new peaks located at 231.4 eV and 228.3 eV indicates the generation of new Mo^{4+} species, providing further evidence for the successful introduction of S.[42] The presence of Mo^{4+} and the formation of oxygen vacancies (O_V) may be attributed to the capture of electrons by Mo^{6+} from the nearby lattice oxygen (O_{Lat}).[43] Specific reactions may be $O_{Lat} - 2e^- \rightarrow 1/2O_2 + O_V^{2+}$ and $Mo^{6+} + 2e^- \rightarrow Mo^{4+}$. The S 2p spectrum (Fig. 3c) exhibited a peak at 163.2 eV attributed to the binding of S_n^{2-} (polysulfide),[44,45] and other peaks at 168.9 eV can be attributed to surface oxidation in air.[46] Notably, forming S_n^{2-} species could induce changes in the metal site's electronic structure and d-band center, thereby promoting the catalytic process.[47]

Furthermore, the O 1s spectrum (Fig. 3d) can be deconvoluted into three peaks. The peak at 530.9 eV can be attributed to an oxygen atom bound to the metal. The peak at 532.4 eV is associated with a hydroxyl species, accompanied by adsorbed water molecules on or near the surface. Finally, the peak observed at 531.7 eV indicates an oxygen vacancy.[48] In addition, the O_V/O_{Lat} on the surface of CoMoO after sulfur doping increased from 0.79 to 1.14. These oxygen vacancies significantly improve the conductivity of the catalyst and accelerate the kinetics of surface redox reactions, thereby enhancing its catalytic performance.[49,50]

3.2 Hydrogen evolution activity

The electrocatalytic activity of the prepared electrocatalysts for the HER in a 1.0 M KOH solution was investigated. The electrocatalytic activity of 20 wt% Pt/C as a baseline catalyst was also measured for comparison. It is well known that Pt/C is the most effective catalyst for the HER in alkaline electrolytes, achieving a current density of 10 mA cm^{-2} (η_{10}) at an overpotential of 32 mV (Fig. 4a). The manipulation of sulfur content serves as a valuable tool for investigating the impact of different sulfur contents on the HER properties. The hydrogen evolution properties of S-CoMoO with differing sulfur doping levels were systematically examined under alkaline conditions. Remarkably, the findings indicate that the sulfur content heavily

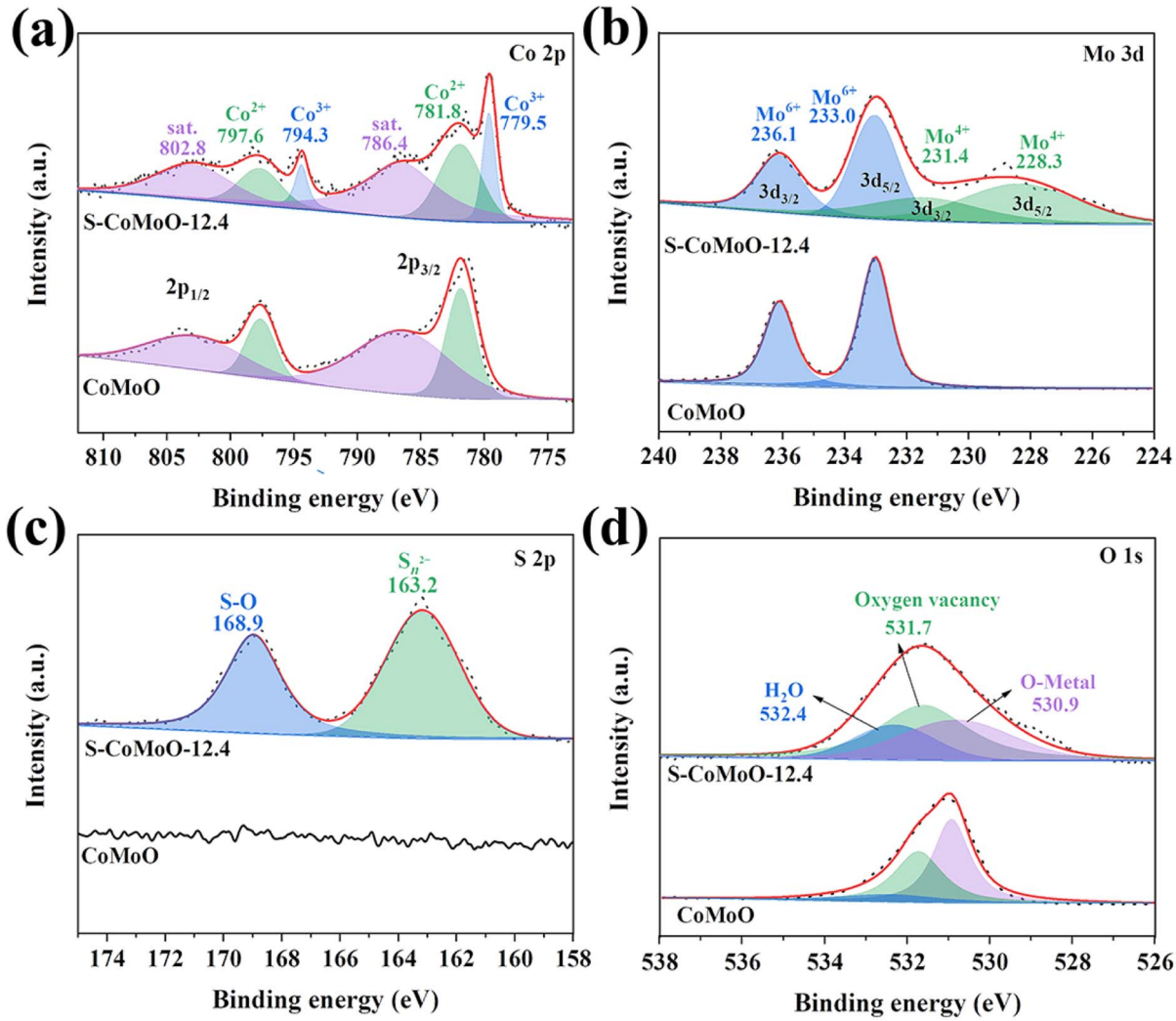

Fig. 3 XPS fine spectra of CoMoO and S-CoMoO-12.4: (a) Co 2p, (b) Mo 3d, (c) S 2p and (d) O 1s.

influences the catalytic activity of S-CoMoO (Fig. 4a). Furthermore, the overpotentials corresponding to a current density of 10 mA cm^{-2} are compiled, exhibiting a characteristic volcano-type curve. Notably, the sulfur doping of S-CoMoO-12.4, which showed the highest HER performance, was determined to be 13.6 at% (Fig. 4b). Additionally, the values of η_{100} (at $j = 100$ mA cm^{-2}) and η_{500} (at $j = 500$ mA cm^{-2}) for the S-CoMoO-12.4 electrode were 218 and 358 mV, respectively, indicating its promising potential as a HER electrocatalyst for commercial electrolyzers.

To investigate the kinetics of the HER, the Tafel plot was employed, with a smaller Tafel slope indicating more favorable reaction kinetics. In agreement with the LSV results, the S-CoMoO-12.4 (Fig. 4c) catalyst exhibited the lowest Tafel slope value of 108.7 mV dec^{-1}, indicating the fastest HER kinetics due to its fast electron transport. Notably, the S-CoMoO-12.4 catalyst exhibited a remarkably low Tafel slope, suggesting that the HER process of this catalyst follows a Volmer–Heyrovsky mechanism.[51] To gain a more comprehensive understanding of the inherent activity of the HER, we conducted a normalization of the TOF of the HER in relation to the number of active sites, as depicted in Fig. S6.† At an overpotential of 300 mV, the TOF of the S-CoMoO-12.4 catalyst was measured to be 2.8×10^{-2} s^{-1}, surpassing the TOF values of CoMoO (1.8×10^{-4} s^{-1}). This observation aligns with the superior HER activity exhibited by the S-CoMoO-12.4 catalyst.

Apart from activity, the stability of electrocatalysts is of utmost importance for practical applications. As shown in Fig. 4d, S-CoMoO-12.4 showed negligible degradation after 40 hours of operating at 10 mA cm^{-2}, highlighting its remarkable stability in the HER process. The LSV curve inset of Fig. 4d indicates only a slight change of 23 mV compared to the initial curve after 40 hours of the HER, further supporting its exceptional stability. Additionally, SEM images (Fig. S7†) reveal that the morphology of S-CoMoO-12.4 remains virtually unchanged following 40 hours of continuous operation. To elucidate the potential chemical structure of CoMoO-12.4 after the HER stability test, the XPS spectra of CoMoO-12.4 before and after the 40 hours stability test were compared. Fig. S8 and S9† show that CoMoO-12.4 after stability testing still shows characteristic

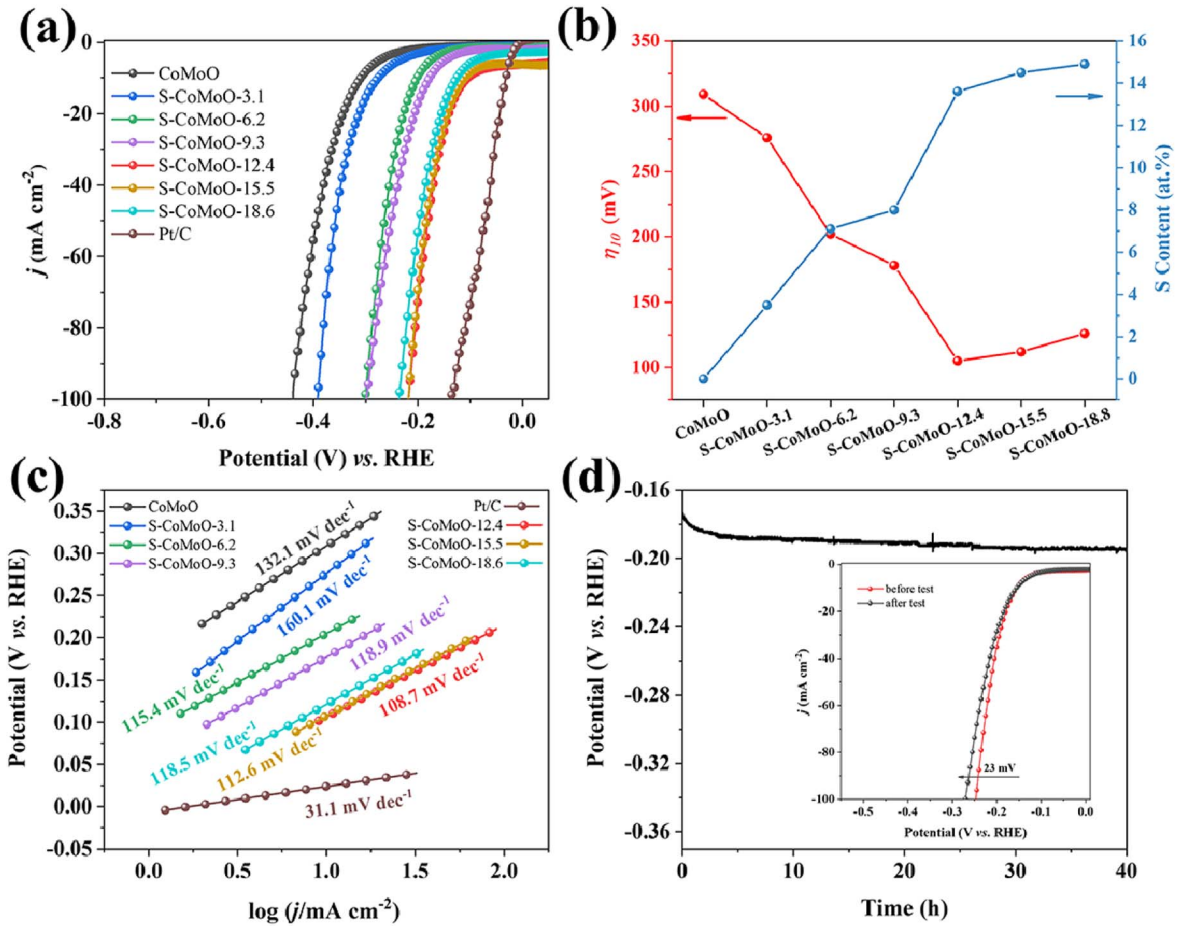

Fig. 4 HER electrocatalytic tests: (a) LSV curves for CoMoO, S-CoMoO-3.1, S-CoMoO-6.2, S-CoMoO-9.3, S-CoMoO-12.4, S-CoMoO-15.5, S-CoMoO-18.6, and Pt/C; (b) η_{10} and (c) Tafel curves of different samples; (d) j–t curves for a duration of 40 h at 10 mA cm^{-2}; inset: the before and after j–t test polarization curves.

peaks corresponding to Co 2p, Mo 3d, S 2p, and O 1s, indicating no significant alteration in chemical composition. However, the absence of the Co^{3+} 2p peak after stability testing can be attributed to the reduction of Co^{3+} to Co^{2+} (Fig. S8a†).

EIS is employed to investigate the kinetic properties of electrodes further. The obtained EIS data (Fig. 5a, S10 and Table S2†) were fitted with an equivalent circuit model. Additionally, the charge transfer resistance (R_{ct}) of CoMoO (10.03 Ω) was found to be significantly higher than that of S-CoMoO-12.4 (2.66 Ω), indicating faster HER kinetics and an expedited faradaic process on the S-CoMoO-12.4 electrode. This can be attributed to the reduced energy barrier for the HER process resulting from the sulfur doping.[47] In addition, the results obtained from EIS fitting (Table S2†) show that the resistances of the equivalent series resistance (R_s) of S-CoMoO-12.4 (1.38 Ω) is smaller than that of CoMoO (1.76 Ω), confirming that sulfur doping can improve the conductivity of CoMoO.

Generally speaking, sulfur-doped electrocatalysts possess a distinct advantage in their high ratio of active catalytic surface sites per unit mass of catalyst material. To demonstrate this advantage, the effective electrochemically active surface area (ECSA) of the S-CoMoO-12.4 electrocatalyst was assessed by cyclic voltammetry (CV) measurements to determine double-layer capacitance (C_{dl}). The ECSA was calculated *via* the equation ECSA = C_{dl}/C_s, where C_s represents the specific capacitance of the sample. This study employed a C_s value of 0.04 mF cm^{-2} based on previously reported data for metal oxides/hydroxides in alkaline solutions.[36] CV curves were acquired at different scan rates (ranging from 10 to 50 mV s^{-1}) within the non-Faraday range (0.281–0.381 V *vs.* RHE) (Fig. S11a and S10b†). The current density (Δj) difference at the intermediate potential (0.33 V) was calculated for each scan rate. The C_{dl} value was determined by calculating the slope of the $\Delta j/2$ *versus* the scan rate curve. Analysis of Fig. S11c† yielded a C_{dl} value of approximately 0.10 mF cm^{-2} for S-CoMoO-12.4, which is higher than that of the CoMoO sample (0.05 mF cm^{-2}), suggesting that S doping could be favorable for exposing more electrochemically active sites in the HER process. Furthermore, it benefits from the hydrangea-like structure with large surface areas and increasingly plentiful exposed edges that afford a mass of active sites for the electrochemical process.[52] The sample's normalized LSV curves (Fig. 5c), obtained from their ECSA measurements, further corroborate that S-CoMoO-12.4 exhibits superior

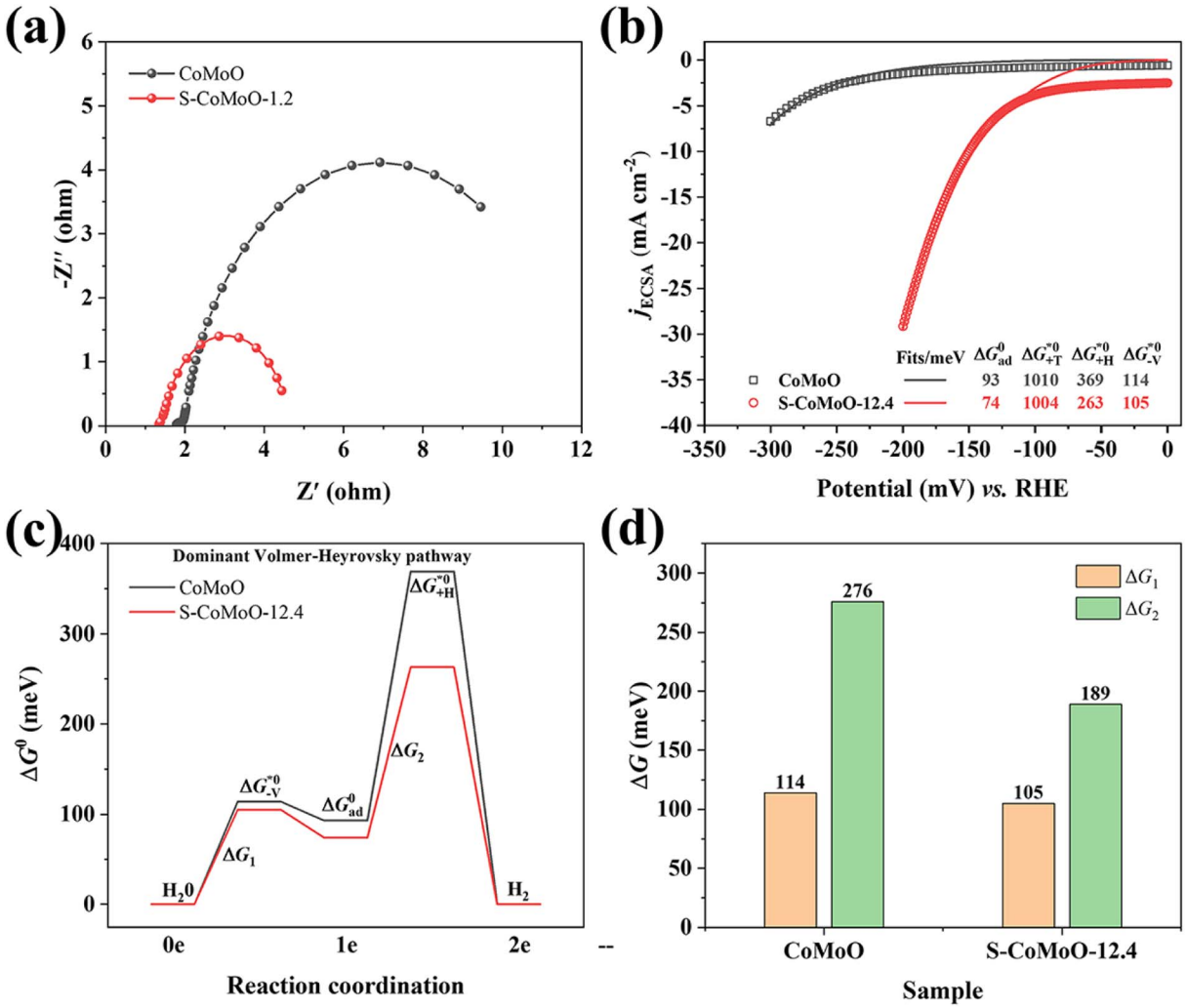

Fig. 5 (a) EIS plots; (b) ECSA normalized polarization curves (symbols) of bare CoMoO and S-CoMoO-12.4 catalysts in 1.0 M KOH solution with the best fits (lines) using the dual-pathway kinetic model. The fitted standard activation free energies are shown with the unit of meV; (c) free energy diagram of the dominant Volmer–Heyrovsky pathway for the HER in alkaline electrolyte for bare CoMoO (grey) and S-CoMoO-12.4 (red) catalysts; (d) ΔG_1 and ΔG_2 of CoMoO and S-CoMoO-12.4. ΔG_1 and ΔG_2 are ΔG^{*0}_{-V} and $\Delta G^{*0}_{+H} - \Delta G^0_{ad}$.

intrinsic HER activity compared to CoMoO, thus confirming that sulfur doping enhances the properties of the active site. Detailed analysis of the actual HER active site will be elaborated in the following sections.

Following Elbert *et al.*'s procedure, we conducted a kinetic analysis to assess the standard activation free energies for the three elementary reaction steps of the HER (for details see the ESI†).[53,54] We utilized the dual-pathway kinetic model to fit the experimental data (from Fig. 5b) of kinetic current density in order to obtain the mechanism and kinetic parameters of the HER.[53,54] The advantage of this method is that it can consider various complex factors and uncertainties in the actual system and more accurately describe the behavior of the real HER. In addition, without the crystallographic information file for CoMoO, we can't do density functional theoretical calculations on it. We constructed a free energy diagram based on the fitted parameters of standard activation free energy. This diagram (Fig. 5c) visually represents the reaction barriers involved in the HER on CoMoO and S-CoMoO-12.4 catalysts. The parameters used in the diagram include ΔG^{*0}_{+T} for the Tafel step, ΔG^{*0}_{-V} for the Volmer step (water dissociation), ΔG^0_{ad} for the standard free energy of adsorption H, and ΔG^{*0}_{+H} for the Heyrovsky step (electrochemical recombination).[53,54] The free energy is lower for the Heyrovsky step than for the Tafel step at 0 V ($\Delta G^{*0}_{+H} < \Delta G^{*0}_{+T}$) (Fig. 5b), indicating that the Volmer–Heyrovsky pathway dominates the HER for both CoMoO and S-CoMoO-12.4.[53,54] The result is in good agreement with the Tafel slope analysis. As shown in Fig. 5c and d, the activation energies on S-CoMoO-12.4 are lower for both the Volmer step ($\Delta G_1 = \Delta G^{*0}_{-V}$) and the Heyrovsky step ($\Delta G_2 = \Delta G^{*0}_{+H} - \Delta G^0_{ad}$) compared to those on bare CoMoO. Specifically, ΔG_1 (S-CoMoO-12.4, 105 meV) < ΔG_1 (CoMoO, 118 meV) and ΔG_2 (S-CoMoO-12.4, 312 meV) < ΔG_2 (CoMoO, 356 meV). This suggests that sulfur doping accelerates the water dissociation and electrochemical recombination steps of the HER in the alkaline environment.

3.3 Oxygen evolution activity and overall water splitting performance

The electrochemical OER performance of the catalysts was also evaluated in 1.0 M KOH using the LSV back-scan method. Fig. 6a presents the LSV curves for the different catalysts, clearly demonstrating the excellent OER performance of the S-CoMoO-12.4 sample. At overpotentials required to maintain current densities of η_{10} and η_{100}, S-CoMoO-12.4 exhibits significantly lower values of 205 mV (η_{10}) and 336 mV (η_{100}), respectively, compared to CoMoO's values of 390 mV (η_{10}) and 491 mV (η_{100}). Moreover, S-CoMoO-12.4 outperforms the noble metal RuO_2 (η_{10} = 298 mV and η_{100} = 573 mV), as depicted in Fig. 6a. Similarly, the impact of sulfur doping on the OER performance mirrors its influence on the HER properties. The sulfur doping of S-CoMoO-12.4, which demonstrated the highest OER performance, was established at 13.6 at% (Fig. 6b). The remarkable catalytic performance of S-CoMoO-12.4 is also evident in its rapid OER kinetics for water oxidation. Incorporating an appropriate amount of sulfur doping is crucial in facilitating the OER process and reducing the energy potential barrier for CoMoO. Fig. S12† shows that the Tafel slope value for S-CoMoO-12.4 is approximately 87.0 mV dec^{-1}, smaller than the value of 92.5 mV dec^{-1} for CoMoO, thus illustrating the enhanced OER kinetics resulting from sulfur incorporation. Additionally, S-CoMoO-12.4 exhibits a smaller R_{ct} value of 0.8 Ω relative to CoMoO (108.8 Ω), indicating excellent charge transfer efficiency (Fig. 6c and Table S3†). To assess the intrinsic OER activity, ECSA-based normalized LSV was conducted, and the results show that S-CoMoO-12.4 possesses a higher inherent OER activity than CoMoO (Fig. S13†). The mass activity (MA) values were then calculated by normalizing the current density to the mass of S-CoMoO-12.4 and comparing them to the respective overpotentials. Fig. S14a† illustrates the MA of the CoMoO and S-CoMoO-12.4 catalysts calculated over the overpotential range of 1.2 to 1.8 V. Notably, at a moderate overpotential of 300 mV, S-CoMoO-12.4 exhibits a MA of 26.60 A g^{-1}, which is 1031 times higher than that of CoMoO (Fig. 6d). Alternatively, the TOF was calculated as another metric of MA to assess intrinsic OER activity. At a sampling overpotential of 300 mV, the TOF of S-CoMoO-12.4 reaches 1.47×10^{-3} s^{-1}, significantly higher than that of the CoMoO (4.29×10^{-6} s^{-1}) sample (Fig. 6d and S14b†). These high MA values confirm that sulfur doping can significantly reduce the material used to achieve efficient catalytic activity. Overall, S-CoMoO-12.4 exhibits a high MA and TOF, showing its superior OER activity. As depicted in Fig. S15,† the C_{dl} of S-CoMoO-12.4 measured at 9.19 mF cm^{-2} exceeded that of CoMoO (1.11 mF cm^{-2}). These results from the experiments suggest that the S-CoMoO-12.4 catalyst possesses a more significant number of active sites.

Fig. 6e shows the long-term durability test of S-CoMoO-12.4 conducted for 40 hours at an applied current density of 10 mA cm^{-2}. Impressively, S-CoMoO-12.4 demonstrates good electrochemical OER stability during this extended testing period. The inset of Fig. 6e clearly shows a minimal shift of 62 mV in the polarization curve of S-CoMoO-12.4 before and after the 40 hours OER test, suggesting remarkable stability. In addition, the high-resolution Co 2p spectra of S-CoMoO-12.4 obtained before and after the OER test (Fig. S16†) confirm significant changes in the oxidation state of cobalt. Notably, the main peaks of Co 2p are positively shifted by about 0.9 eV to 780.4 and 779.5 eV. These energy shifts can be attributed to CoOOH species, which are identified as the active centers for the OER process.[55] In addition, the decay of the characteristic satellite peak of Co^{2+} proves the conversion of Co^{2+} to the CoOOH active center during OER catalysis. Furthermore, the SEM image in Fig. S17† indicates that the morphology of S-CoMoO-12.4 exhibits minimal alteration even after 40 hours of uninterrupted operation.

The S-CoMoO-12.4 catalyst demonstrates favorable electrocatalytic performance in both the HER and OER. To showcase the potential application of S-CoMoO-12.4 in overall water splitting, a two-electrode electrolyzer employs S-CoMoO-12.4 as both the anode and cathode materials. For comparative purposes, a commercial cell consisting of RuO_2 (anode) and 20 wt% Pt/C (cathode) is also employed. The S-CoMoO-12.4‖S-CoMoO-12.4 system exhibits a remarkable current density of 10 mA cm^{-2} at a cell voltage of only 1.61 V (Fig. 6d). Surprisingly, as the current density is 100 mA cm^{-2}, the required overpotential of our S-CoMoO-12.4‖S-CoMoO-12.4 system (1.80 V) is even lower than that of the commercial 20 wt% Pt/C‖RuO_2 cell (1.89 V). Furthermore, the long-term durability of the S-CoMoO-12.4 catalyst for overall water splitting is confirmed by a negligible degradation of only 23 mV after 1000 cycles (Fig. S18†). These findings unequivocally establish the S-CoMoO-12.4 composite as a highly efficient electrocatalyst for water splitting.

3.4 Mechanisms of the HER and OER

Overall, we summarize the key electrochemical indicators (such as $1/R_s$, ECSA, and TOF values) of CoMoO and S-CoMoO-12.4 in a radar chart to demonstrate the comprehensive advantages of sulfur-doped catalysts (Fig. 7a). The smaller R_s implies better electronic conductivity, which suggests faster electron transfer rates in the solution, contributing to the improved activity and efficiency of the catalyst. Furthermore, as mentioned earlier, sulfur doping reduces the R_{ct} of CoMoO, thereby decreasing the degree of electrochemical reaction polarization and increasing its charge transfer rate, resulting in faster reaction rates. Fig. 7a shows that sulfur doping can increase the ECSA of CoMoO, providing more reaction sites for the HER or OER. Additionally, sulfur doping can also enhance the TOF value of CoMoO, where higher TOF values indicate better intrinsic activity of the catalyst. Additionally, the electrocatalytic activity of S-CoMoO-12.4 surpasses that of most non-noble metal-based oxide catalysts recently reported, as depicted in Fig. 7b and Table S4.†

To investigate the underlying mechanism of activity enhancement, we conducted XPS characterization of CoMoO and S-CoMoO-12.4 samples after HER or OER testing. Firstly, we analyzed the potential mechanism of HER activity enhancement. The Co 2p spectra of all samples after the HER showed two sets of peaks, where 781.8 and 797.6 eV corresponded to Co^{2+} and 786.4 and 802.8 eV corresponded to satellite peaks

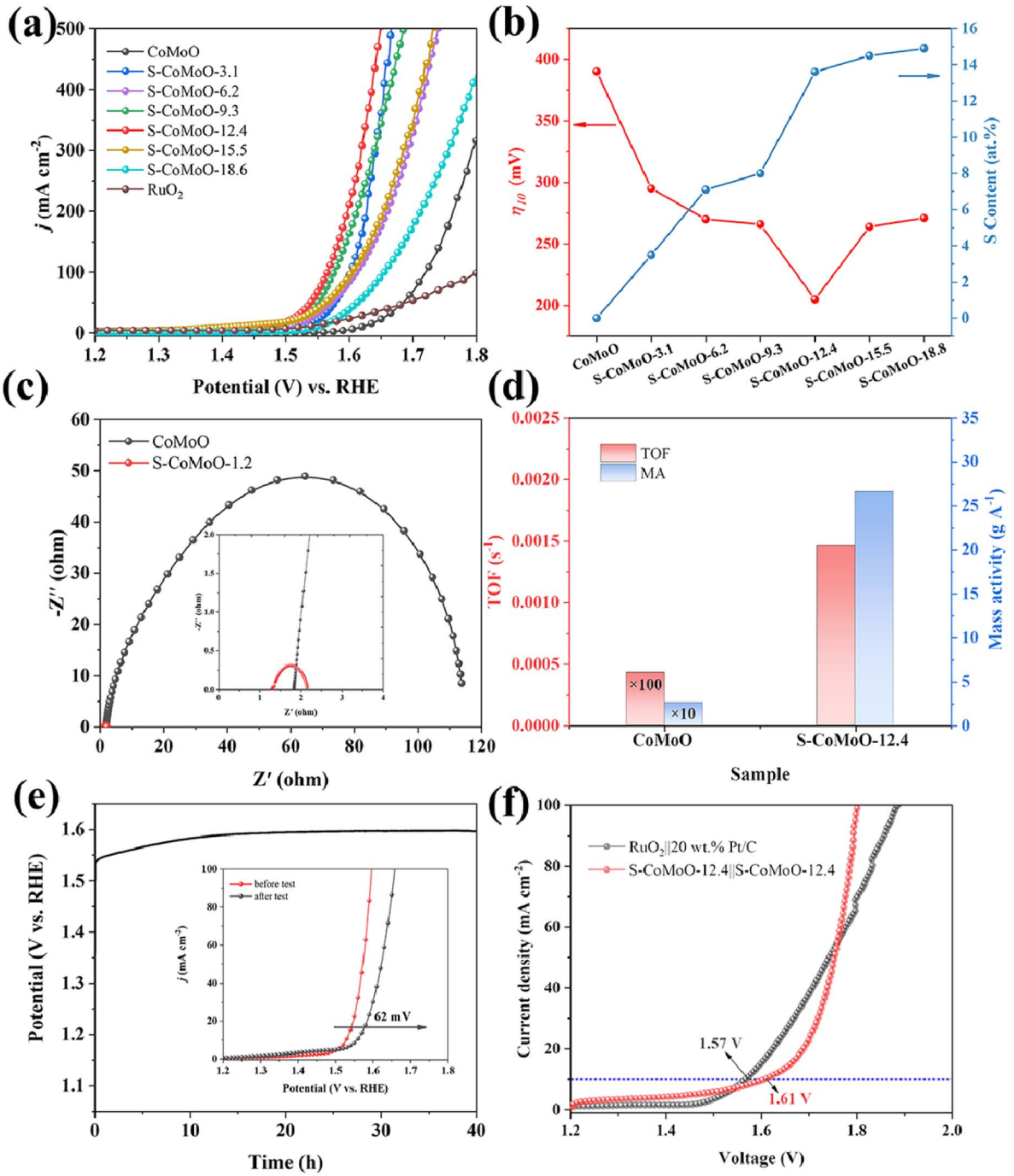

Fig. 6 OER electrocatalytic tests: (a) LSV curves for CoMoO, S-CoMoO-3.1, S-CoMoO-6.2, S-CoMoO-9.3, S-CoMoO-12.4, S-CoMoO-15.5, S-CoMoO-18.6, and RuO_2, (b) η_{10} of different samples, (c) EIS plots and (d) TOF and MA for CoMoO and S-CoMoO-12.4 at $\eta = 300$ mV (1.53 V *vs.* RHE); (e) *j*–*t* curves for a duration of 40 h at 10 mA cm^{-2}; inset: the before and after *j*–*t* test polarization curves; (f) LSV curves of the electrolyzer.

(Fig. S19 and S20†). The disappearance of the Co^{3+} peak in the initial S-CoMoO-12.4 (Fig. S19†) indicated that Co^{3+} in S-CoMoO-12.4 may have been reduced to Co^{2+} during the HER. The Mo 3d spectra of both samples after the HER (Fig. S19 and S20†) were similar to those before testing, but only the S-CoMoO-12.4 sample contained a Mo^{4+} peak (228.3 and 231.4 eV). After HER testing, the Mo^{4+} content in S-CoMoO-12.4 increased from 49.73% to 62.75%, suggesting that some of the Mo^{6+} in S-CoMoO-12.4 was reduced (Fig. 7c and Table S5†). The unsaturated Mo^{4+} sites can achieve electron focusing on the Mo site, thereby enhancing the adsorption of H_2O.[56,57]

In addition, the O 1s spectra of S-CoMoO-12.4 after HER testing (Fig. S19 and S20†) showed a higher H_2O peak content (25.77%) compared to CoMoO (19.73%), further confirming this

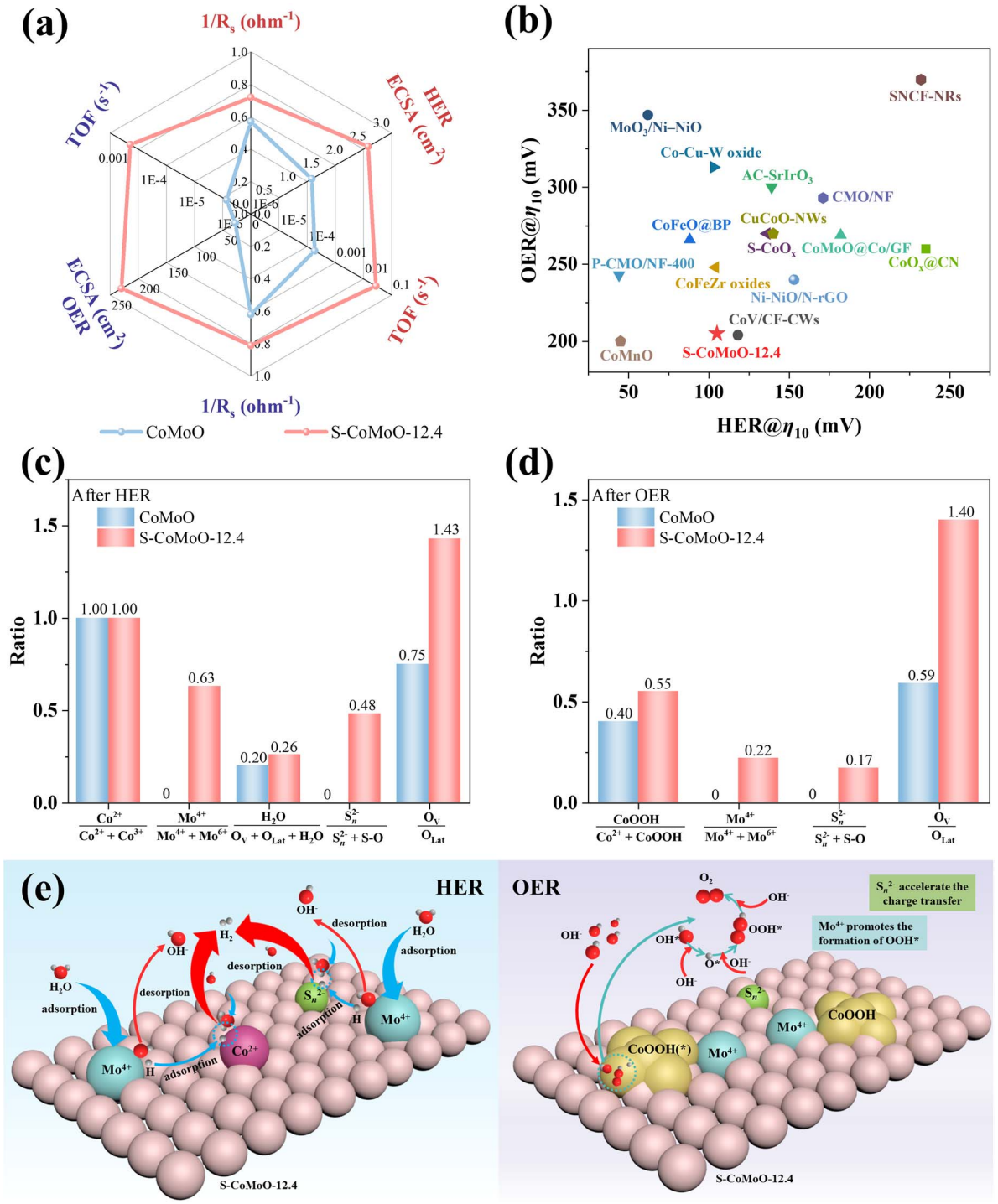

Fig. 7 (a) Radar chart for comparing the comprehensive performances of CoMoO and S-CoMoO-12.4; (b) comparison of overpotential (10 mA cm^{-2}) for non-noble metal-based oxide electrocatalysts in alkaline medium; summary chart of the proportions of CoMoO and S-CoMoO-12.4 in different components after the HER (c) and OER (d); (e) electrochemical HER and OER potential mechanism diagram of S-CoMoO-12.4. The structure depicted in the figure is intended to serve as a schematic representation rather than an actual structural diagram.

observation. Furthermore, the O_v/O_{Lat} value of S-CoMoO-12.4 after HER testing (1.43) was higher than that of CoMoO (0.75), indicating that S-CoMoO-12.4 had more oxygen vacancies after HER testing (Fig. 7c). In transition metal oxides, abundant O_v can enhance electronic conductivity and facilitate water dissociation, significantly promoting the alkaline HER reaction kinetics.[58–60] As mentioned above, a large number of O_v in the catalyst are highly beneficial for promoting alkaline HER. Moreover, bridging S_n^{2-} species is believed to serve as active sites for the HER, owing to their moderate Gibbs free energy for

atomic hydrogen adsorption.[61–63] Based on the above results, we propose the potential mechanism of the HER on S-CoMoO-12.4, as illustrated in Fig. 7e. Specifically, the process begins with the initial adsorption of H_2O molecules on Mo^{4+} sites, which is followed by the subsequent splitting of water into hydroxide ions (OH^-) and hydrogen (H) atoms (hydrogen absorption). The H atoms then migrate to adjacent Co^{2+} or S_n^{2-} sites and ultimately recombine to form H_2, while the OH^- desorbs from Mo^{4+} or S_n^{2-} sites (electrochemical hydrogen desorption).

The Co 2p spectra of all samples were obtained after OER testing to investigate the potential mechanism of OER activity enhancement (Fig. S21 and S22†). The spectra showed three sets of different peaks, with peaks at 781.8 and 797.6 eV corresponding to Co^{2+}, peaks at 780.4 and 795.6 eV corresponding to CoOOH, and peaks at 786.4 and 802.8 eV corresponding to satellite peaks (Fig. S21 and S22†). The appearance of the CoOOH peak in the OER process was attributed to the oxidation of Co^{2+}. Furthermore, the CoOOH/(Co^{2+} + CoOOH) value of S-CoMoO-12.4 (54.75%) after OER testing was higher than that of CoMoO (39.66%), indicating that S-CoMoO-12.4 contained more OER active species (CoOOH) after OER testing. The Mo 3d spectra of both samples after OER testing (Fig. S21, S22 and Table S5†) were similar to those before testing, but only the S-CoMoO-12.4 sample contained a Mo^{4+} peak (228.3 and 231.4 eV). Compared to before OER testing, the Mo^{4+} content in S-CoMoO-12.4 decreased from 49.73% to 21.96%, indicating that Mo^{4+} in S-CoMoO-12.4 was partially oxidized during the OER. Mo^{4+} can attract electrons from oxygen evolution intermediates (OOH*), promoting their formation and stabilization, and increasing oxygen release.[64]

Furthermore, the O_v/O_{Lat} value of S-CoMoO-12.4 (1.40) after OER testing (Fig. 7d, S21 and S22†) was higher than that of CoMoO (0.59), indicating that S-CoMoO-12.4 had more O_v after OER testing. O_v can facilitate the surface reconstruction of transition metal oxides into metal hydroxides, thereby promoting the OER.[65] The S_n^{2-} can accelerate the charge transfer, thereby promoting the OER catalytic process.[66] Additionally, the strong chemical bond of S_n^{2-} in S-CoMoO-12.4 can improve electrochemical stability and accelerate the charge transfer process of S-CoMoO-12.4. Previous studies have demonstrated that transferring electrons from metals to heteroatoms can weaken metal bonds, thereby reducing the energy barrier for forming intermediates and enhancing OER activity.[67–69] Based on the results above, the OER mechanism of S-CoMoO-12.4 may involve the adsorbate evolution mechanism, which encompasses a four-step synergistic electron transfer cycle for oxygen generation, as illustrated in Fig. 7e. The superior OER performance of S-CoMoO-12.4 can be ascribed to the synergistic effect of its CoOOH, Mo^{4+}, and S_n^{2-} constituents. The presence of Mo^{4+} facilitates the attraction of electrons from the OER intermediates, thereby contributing to the stabilization of the OER intermediates and consequently promoting oxygen generation on CoOOH active sites. Additionally, the inclusion of S_n^{2-} is found to accelerate the charge transfer in the OER process. These combined effects collectively contribute to the remarkable OER performance observed in S-CoMoO-12.4.

Overall, the exceptional bi-functional activity and stability of S-CoMoO-12.4 can be attributed to several key factors. Firstly, the unique hydrangea structure exhibits a larger surface area and an increased number of exposed edges, which provide abundant active sites for electrochemical processes. Secondly, the introduction of S-doping alters the electronic structure of CoMoO, leading to improved conductivity and facilitating electron transfer. Thirdly, the presence of unsaturated Mo^{4+} sites enhances the adsorption of H_2O molecules, thereby facilitating the HER. The Mo^{4+} species in the catalyst can also attract electrons from the OER intermediates, significantly enhancing the OER activity. Fourth, the existence of S_n^{2-} species promotes both the HER and OER processes. It serves as the active site of the HER and also accelerates the charge transfer in the OER process. Lastly, O_v plays a critical role in enhancing the catalytic performance of transition metal oxides. Specifically, O_v promotes the restructuring of transition metal oxide surfaces into metal hydroxides, thereby facilitating the OER. Moreover, the abundance of O_v enhances electronic conductivity and facilitates water dissociation, thereby significantly influencing the kinetics of alkaline HER. Collectively, these factors synergistically influence the rate and efficiency of electrochemical reactions, playing a crucial role in improving the activity and efficiency of the catalyst.

4. Conclusions

In conclusion, a sulfur-doped CoMoO electrocatalyst with a hydrangea-like structure was successfully synthesized *in situ* on CFP substrates *via* a facile one-step hydrothermal method. The hydrangea-like structure provides abundant active sites and facilitates rapid mass transfer. The optimum S-CoMoO-12.4 catalyst exhibited remarkable catalytic activity and stability for both the HER and OER in alkaline solutions. It requires only 105 and 205 mV overpotentials at 10 mA cm^{-2} for the HER and OER. The exceptional catalytic performance of S-CoMoO-12.4 can be attributed to a combination of factors. Specifically, the presence of unsaturated Mo^{4+} sites enhances the adsorption of H_2O molecules, thereby promoting the formation of H_2 at the Co^{2+} or S_n^{2-} site. The Mo^{4+} species can attract electrons from the OER intermediates, thereby promoting the formation of O_2 at the active center of CoOOH. In addition, the presence of S_n^{2-} can accelerate charge transfer during the OER. The cell voltage for the electrolyzer was only 1.61 V at 10 mA cm^{-2} under the alkaline conditions. In this study, we have elucidated the distinct catalytic mechanisms of sulfur doping for enhancing the HER and OER activities of CoMoO water splitting catalysts. These findings offer valuable insights for developing high-performance bi-functional water splitting catalysts.

Conflicts of interest

There are no conflicts to declare.

Acknowledgements

Z. Huang acknowledges the support from the National Natural Science Foundation of China (62275197 and 51772214), the Natural Science Foundation of Shanghai (23ZR1465700), the

National Youth Talent Support Program of China (W03070073), and the Fundamental Research Funds for the Central Universities. M. G. Humphrey thanks the Australian Research Council (DP170100411). C. Zhang acknowledges support from the National Natural Science Foundation of China (51432006), the Ministry of Education of China (IRT14R23), the 111 Project (B13025), and the Innovation Program of Shanghai Municipal Education Commission.

References

1 C. L. Wang and D. Astruc, *Chem. Soc. Rev.*, 2021, **50**, 3437–3484.
2 G. Glenk and S. Reichelstein, *Nat. Energy*, 2019, **4**, 216–222.
3 B. You and Y. J. Sun, *Acc. Chem. Res.*, 2018, **51**, 1571–1580.
4 X. Luo, P. X. Ji, P. Y. Wang, X. Tan, L. Chen and S. C. Mu, *Adv. Sci.*, 2022, **9**, 2104846.
5 Y. J. Son, K. Kawashima, B. R. Wygant, C. H. Lam, J. N. Burrow, H. Celio, A. Dolocan, J. G. Ekerdt and C. B. Mullins, *ACS Nano*, 2021, **15**, 3468–3480.
6 Y. Ding, K. W. Cao, J. W. He, F. M. Li, H. Huang, P. Chen and Y. Chen, *Chin. J. Catal.*, 2022, **43**, 1535–1543.
7 Q. Xue, X. Y. Bai, Y. Zhao, Y. N. Li, T. J. Wang, H. Y. Sun, F. M. Li, P. Chen, P. J. Jin, S. B. Yin and Y. Chen, *J. Energy Chem.*, 2022, **65**, 94–102.
8 C. Xu, M. Y. Zhang, X. J. Yin, Q. Gao, S. Jiang, J. Y. Cheng, X. Kong, B. Liu and H. Q. Peng, *J. Mater. Chem. A*, 2023, **11**, 18502–18529.
9 J. Zhao, N. Liao and J. S. Luo, *J. Mater. Chem. A*, 2023, **11**, 9682–9690.
10 J. G. Hou, Y. Z. Wu, B. Zhang, S. Y. Cao, Z. W. Li and L. C. Sun, *Adv. Funct. Mater.*, 2019, **29**, 1808367.
11 H. J. Zhang, A. W. Maijenburg, X. P. Li, S. L. Schweizer and R. B. Wehrspohn, *Adv. Funct. Mater.*, 2020, **30**, 2003261.
12 Y. W. Deng, Y. F. Cao, Y. Xia, X. Y. Xi, Y. Wang, W. F. Jiang, D. Yang, A. G. Dong and T. T. Li, *Adv. Energy Mater.*, 2022, **12**, 2202394.
13 C. L. Chen, M. R. Sun, K. X. Wang and Y. J. Li, *SmartMat*, 2022, **3**, 533–564.
14 J. Z. Li, C. Chen, L. K. Xu, Y. Zhang, W. Wei, E. R. Zhao, Y. Wu and C. Chen, *JACS Au*, 2023, **3**, 736–755.
15 T. Wu, E. H. Song, S. N. Zhang, M. J. Luo, C. D. Zhao, W. Zhao, J. J. Liu and F. Q. Huang, *Adv. Mater.*, 2022, **34**, 2108505.
16 L. Zhang, C. J. Lu, F. Ye, Z. Y. Wu, Y. A. Wang, L. Jiang, L. Zhang, C. Cheng, Z. M. Sun and L. F. Hu, *Appl. Catal., B*, 2021, **284**, 119758.
17 X. Y. Lu and C. A. Zhao, *Nat. Commun.*, 2015, **6**, 1–7.
18 F. S. Farahani, M. S. Rahmanifar, A. Noori, M. F. El-Kady, N. Hassani, M. Neek-Amal, R. B. Kaner and M. F. Mousavi, *J. Am. Chem. Soc.*, 2022, **144**, 3411–3428.
19 M. Moloudi, A. Noori, M. S. Rahmanifar, Y. Shabangoli, M. F. El-Kady, N. B. Mohamed, R. B. Kaner and M. F. Mousavi, *Adv. Energy Mater.*, 2023, **13**, 2203002.
20 Y. Y. Guo, P. F. Yuan, J. A. Zhang, H. C. Xia, F. Y. Cheng, M. F. Zhou, J. Li, Y. Y. Qiao, S. C. Mu and Q. Xu, *Adv. Funct. Mater.*, 2018, **28**, 1805641.
21 Y. Yuan, J. H. Wang, S. Adimi, H. J. Shen, T. Thomas, R. G. Ma, J. P. Attfield and M. H. Yang, *Nat. Mater.*, 2020, **19**, 282–286.
22 P. Y. Wang, T. T. Wang, R. Qin, Z. H. Pu, C. T. Zhang, J. W. Zhu, D. Chen, D. Feng, Z. K. Kou, S. C. Mu and J. Wang, *Adv. Energy Mater.*, 2022, **12**, 2103359.
23 Y. Gao, Y. R. Xue, T. F. Liu, Y. X. Liu, C. Zhang, C. Y. Xing, F. He and Y. L. Li, *Adv. Sci.*, 2021, **8**, 2102777.
24 W. H. Luo, Y. Wang, L. X. Luo, S. Gong, M. N. Wei, Y. X. Li, X. P. Gan, Y. Y. Zhao, Z. H. Zhu and Z. Li, *ACS Catal.*, 2022, **12**, 1167–1179.
25 S. Sanati, A. Morsali and H. Garcia, *Energy Environ. Sci.*, 2022, **15**, 3119–3151.
26 Q. Quan, Y. X. Zhang, F. Wang, X. M. Bu, W. Wang, Y. Meng, P. S. Xie, D. Chen, W. J. Wang, D. J. Li, C. T. Liu, S. Yip and J. C. Hoa, *Nano Energy*, 2022, **101**, 107566.
27 S. W. Zhang, B. S. Yin, X. X. Liu, D. M. Gu, H. Gong and Z. B. Wang, *Nano Energy*, 2019, **59**, 41–49.
28 S. Y. Zhao, J. Berry-Gair, W. Y. Li, G. Q. Guan, M. N. Yang, J. W. Li, F. L. Lai, F. Cora, K. Holt, D. J. L. Brett, G. J. He and I. P. Parkin, *Adv. Sci.*, 2020, **7**, 1903674.
29 G. Y. Zhou, M. Li, Y. L. Li, H. Dong, D. M. Sun, X. Liu, L. Xu, Z. Q. Tian and Y. W. Tang, *Adv. Funct. Mater.*, 2020, **30**, 1905252.
30 Y. G. Zhao, W. C. Wan, N. Dongfang, C. A. Triana, L. Douls, C. Huang, R. Erni, M. Iannuzzi and G. R. Patzke, *ACS Nano*, 2022, **16**, 15318–15327.
31 Z. Zhao, Z. K. Yuan, Z. S. Fang, J. H. Jian, J. Li, M. J. Yang, C. S. Mo, Y. Zhang, X. H. Hu, P. Li, S. Y. Wang, W. Hong, Z. K. Zheng, G. F. Ouyang, X. D. Chen and D. S. Yu, *Adv. Sci.*, 2018, **5**, 1800760.
32 S. J. Peng, X. P. Han, L. L. Li, S. L. Chou, D. X. Ji, H. J. Huang, Y. H. Du, J. Liu and S. Ramakrishna, *Adv. Energy Mater.*, 2018, **8**, 1800612.
33 X. R. Li, J. L. Wei, Q. Li, S. S. Zheng, Y. X. Xu, P. Du, C. Y. Chen, J. Y. Zhao, H. G. Xue, Q. Xu and H. Pang, *Adv. Funct. Mater.*, 2018, **28**, 1800886.
34 Z. S. Li, L. Lv, J. S. Wang, X. Ao, Y. J. Ruan, D. C. Zha, G. Hong, Q. H. Wu, Y. C. Lan, C. D. Wang, J. J. Jiang and M. L. Liu, *Nano Energy*, 2018, **47**, 199–209.
35 J. Wang, J. Hu, C. Liang, L. M. Chang, Y. C. Du, X. J. Han, J. M. Sun and P. Xu, *Chem. Eng. J.*, 2022, **446**, 137094.
36 Y. H. Zhao, Y. Z. Wang, Y. T. Dong, C. Carlos, J. Li, Z. Y. Zhang, T. Li, Y. Shao, S. Yan, L. Gu, J. Wang and X. D. Wang, *ACS Energy Lett.*, 2021, **6**, 3367–3375.
37 D. Guo, M. Y. Zhang, Z. Chen and X. X. Liu, *RSC Adv.*, 2018, **8**, 33374–33382.
38 Y. Zhang, Q. Shao, S. Long and X. Q. Huang, *Nano Energy*, 2018, **45**, 448–455.
39 L. C. Xia, J. P. Wang, L. L. Bo, W. P. Shi, Y. I. Zhang, Y. X. Shen, X. C. Ji, X. L. Guan, Y. X. Wang and J. H. Tong, *Chem. Eng. J.*, 2023, **467**, 143464.
40 F. X. Xie, W. C. H. Choy, C. D. Wang, X. C. Li, S. Q. Zhang and J. H. Hou, *Adv. Mater.*, 2013, **25**, 2051–2055.
41 R. D. Wang, F. Li, J. Ji and F. Wang, *Appl. Surf. Sci.*, 2022, **579**, 152128.

42 Z. Z. Liu, X. Shang, B. Dong and Y. M. Chai, *J. Catal.*, 2018, **361**, 204–213.
43 Q. H. Wu, L. Y. Chen, D. H. Kuo, P. Li, A. B. Abdeta, O. A. Zelekew, J. G. Lin and X. Y. Chen, *ACS Appl. Mater. Interfaces*, 2023, **15**, 22142–22156.
44 D. M. Feng, S. S. Zhang, Y. Tong and X. P. Dong, *J. Colloid Interface Sci.*, 2022, **623**, 467–475.
45 V. Malgras, A. Nattestad, Y. Yamauchi, S. X. Dou and J. H. Kim, *Nanoscale*, 2015, **7**, 5706–5711.
46 R. Z. Chen, Z. Y. Zhang, Z. C. Wang, W. Wu, S. W. Du, W. B. Zhu, H. F. Lv and N. C. Cheng, *ACS Catal.*, 2022, **12**, 13234–13246.
47 Y. Huang, L. W. Jiang, H. Liu and J. J. Wang, *Chem. Eng. J.*, 2022, **441**, 136121.
48 L. Lei, Z. Yin, D. L. Huang, Y. S. Chen, S. Chen, M. Cheng, L. Du and Q. H. Liang, *J. Colloid Interface Sci.*, 2022, **612**, 413–423.
49 F. Y. Cheng, T. R. Zhang, Y. Zhang, J. Du, X. P. Han and J. Chen, *Angew. Chem., Int. Ed.*, 2013, **52**, 2474–2477.
50 X. F. Lu, L. F. Gu, J. W. Wang, J. X. Wu, P. Q. Liao and G. R. Li, *Adv. Mater.*, 2017, **29**, 1604437.
51 X. K. Huang, X. P. Xu, C. Li, D. F. Wu, D. J. Cheng and D. P. Cao, *Adv. Energy Mater.*, 2019, **9**, 1803970.
52 X. Zhang, Y. Xue, Q. Yan, K. Zhu, K. Ye, J. Yan, D. Cao, X. Huang and G. Wang, *Mater. Today Energy*, 2021, **21**, 100741.
53 K. Elbert, J. Hu, Z. Ma, Y. Zhang, G. Y. Chen, W. An, P. Liu, H. S. Isaacs, R. R. Adzic and J. X. Wang, *ACS Catal.*, 2015, **5**, 6764–6772.
54 J. Hu, C. X. Zhang, L. Jiang, H. Lin, Y. M. An, D. Zhou, M. K. H. Leung and S. H. Yang, *Joule*, 2017, **1**, 383–393.
55 W. Hua, H. Sun, L. Ren, Y. Li and J. G. Wang, *Chem. Eng. J.*, 2021, **420**, 129717.
56 J. Sun, S. Qin, Z. Zhang, C. Li, X. Xu, Z. Li and X. Meng, *Appl. Catal., B*, 2023, **338**, 123015.
57 Y. Zhou, Y. M. Wang, D. Q. Kong, Q. Q. Zhao, L. Zhao, J. L. Zhang, X. M. Chen, Y. A. Li, Y. Xu and C. Meng, *Adv. Funct. Mater.*, 2023, **33**, 2210656.
58 J. Carrasco, D. López-Durán, Z. Y. Liu, T. Duchon, J. Evans, S. D. Senanayake, E. J. Crumlin, V. Matolín, J. A. Rodríguez and M. V. Ganduglia-Pirovano, *Angew. Chem., Int. Ed.*, 2015, **54**, 3917–3921.
59 M. Molinari, S. C. Parker, D. C. Sayle and M. S. Islam, *J. Phys. Chem. C*, 2012, **116**, 7073–7082.
60 T. Zhang, M. Y. Wu, D. Y. Yan, J. Mao, H. Liu, W. B. Hu, X. W. Du, T. Ling and S. Z. Qiao, *Nano Energy*, 2018, **43**, 103–109.
61 L. R. L. Ting, Y. L. Deng, L. Ma, Y. J. Zhang, A. A. Peterson and B. S. Yeo, *ACS Catal.*, 2016, **6**, 861–867.
62 Y. Y. Fan, Y. F. Sun, X. Zhang and J. X. Guo, *Chem. Eng. J.*, 2021, **426**, 131922.
63 C. Wang, T. Y. Wang, J. J. Liu, Y. Zhou, D. W. Yu, J. K. Cheng, F. Han, Q. Li, J. T. Chen and Y. H. Huang, *Energy Environ. Sci.*, 2018, **11**, 2467–2475.
64 B. C. Moon, W. H. Choi, K. H. Kim, D. G. Park, J. W. Choi and J. K. Kang, *Small*, 2019, **15**, 1804764.
65 H. B. Xiao, K. Chi, H. X. Yin, X. J. Zhou, P. X. Lei, P. Z. Liu, J. K. Fang, X. H. Li, S. L. Yuan, Z. Zhang, Y. Q. Su, J. J. Guo and L. H. Qian, *Energy Environ. Mater.*, 2023, e12495.
66 Y. Huang, L. W. Jiang, H. Liu and J. J. Wang, *Chem. Eng. J.*, 2022, **441**, 136121.
67 K. Kim, T. Kang, M. Kim and J. Kim, *Chem. Eng. J.*, 2021, **426**, 130820.
68 H. Ren, X. L. Sun, C. F. Du, J. Zhao, D. B. Liu, W. Fang, S. Kumar, R. Chua, S. Z. Meng, P. Kidkhunthod, L. Song, S. Q. Li, S. Madhavi and Q. Y. Yan, *ACS Nano*, 2019, **13**, 12969–12979.
69 J. W. Hall, N. Membreno, J. Wu, H. Celio, R. A. Jones and K. J. Stevenson, *J. Am. Chem. Soc.*, 2012, **134**, 5532–5535.